Solid State Sciences 133 (2022) 107021

Contents lists available at ScienceDirect

Solid State Sciences

journal homepage: www.elsevier.com/locate/ssscie

Effect of chlorine doping on some physical properties of annealed In_2S_3 thin layers deposited by spray technique

M. Toumi [a], N. Bouguila [a], B. Tiss [a], C. Dias [b,*], R.C. Veloso [b], M. Kraini [a], J. Ventura [b], S. Alaya [a]

[a] Laboratory of Physics of Materials and Nanomaterials Applied at Environment, Faculty of Sciences in Gabes, Gabes University, 6072, Gabes, Tunisia
[b] IFIMUP, Departamento de Física e Astronomia, Faculdade de Ciências, Universidade Do Porto, Rua Do Campo Alegre S/n, 4169–007 Porto, Portugal

A B S T R A C T

Indium sulfide (In_2S_3) is a promising semiconductor that it is known as a candidate material for optoelectronic devices and applications owing to its exceptional electrical and optical properties. Here, we used the spray pyrolysis process to deposit undoped, and chlorine doped In_2S_3 films. Then, the as-prepared samples were exposed to heat treatment in a furnace at 400 °C for 1 h. The structural measurements reveal that the obtained samples show a polycrystalline nature with the formation of β-In_2S_3 cubic structure. Besides, the In_2O_3 appears as a secondary phase for undoped In_2S_3 and gradually disappears with the increase of level doping. The formation of In_2O_3 from In_2S_3 is inversely proportional to the evolution of the chlorine concentration. The EDS analysis reveals the constituent elements In and S of the undoped layer and indicates that the material is sulfur deficient. The forbidden energy of In_2S_3 is ranging from 2.59 to 2.92 eV. These results prove that our material is suitable for interesting application such as thin film solar cell, buffer layer and transparent conductive oxide (TCO).

1. Introduction

In recent times, In_2S_3 has been among the most widely used materials in the manufacturing of the solar cell component. The best-known properties are as an n-type semiconductor with non-toxic constituents and a direct wide bandgap (2.0–3.2 eV) [1]. As well as its chemical stability, photoconductive nature and high transparent in the visible range, make In_2S_3 an alternative to cadmium sulfide toxic buffer layer [2]. Overall, In_2S_3 has three crystallographic phases which are: α phase, β phase and γ phase. Noting that, the β phase of In_2S_3 is the most stable one in room temperature [3]. In order to synthesize In_2S_3 layers different processes were used like: RF sputtering [4], thermal evaporation [5], chemical bath deposition [6], electroplating [7] and ultrasonic pyrolysis [8]. Moreover, the physicochemical properties of this material could be adjusted via different ways like doping, heat treatment and etching. In order to enhance the physical properties, a post deposition annealing treatment is required [1,9]. It is interesting to note that several research groups resort to the doping of In_2S_3 films to improve their structural, morphological and optical properties. Namely, Tiss et al. determined that introducing silver resulted in an improvement in the crystallinity and conductivity of the samples [10]. Kim et al. noted that cobalt doped samples show a reduction in the defects [11]. Others found that aluminium doping increased the oxygen adsorption in the samples [12], and the introduction of sodium resulted in a bandgap widening in addition to enormous and better conductivity [13]. Chlorine is a promising doping material since it has been shown to increase the photosensitivity and crystallinity of In_2S_3 [14]. John et al. reported that the activation energy of the Cl^- doped In_2S_3 layer is about 3 times than that of the original layer, which means that the former constant is 6 times than that of the In_2S_3 layer without Cl [15]. According to reports, the use of Cl^- based precursors can produce highly crystalline and light-sensitive In_2S_3 films as an effective compensation mechanism to replace cadmium telluride (CdTe) films, as a non-toxic material for solar cell applications [16]. Annealing effects on the structural, optical, and morphological properties have been studied by various research groups. The main idea is that thin film crystallinity improves when the annealing temperature increases, thankful to reduction of structural film defects [17,18]. In addition, the surface finish improves as the surface smoothness increases when the annealing temperature increases while the band energy decreases [19,20].

The present study focuses particularly on the impact of air annealing treatment on: structural, morphological and optical properties of In_2S_3films deposited by spray pyrolysis on glass substrates. The deposited films have been subjected to heat treatment for 1 h at 400 °C.

2. Experimental study

2.1. Preparation of indium sulfide layers

Our protocol of synthesize consists of dissolving 0.1504 g of indium

* Corresponding author.
E-mail address: c.dias@fc.up.pt (C. Dias).

https://doi.org/10.1016/j.solidstatesciences.2022.107021
Received 1 April 2022; Received in revised form 7 September 2022; Accepted 16 September 2022
Available online 21 September 2022

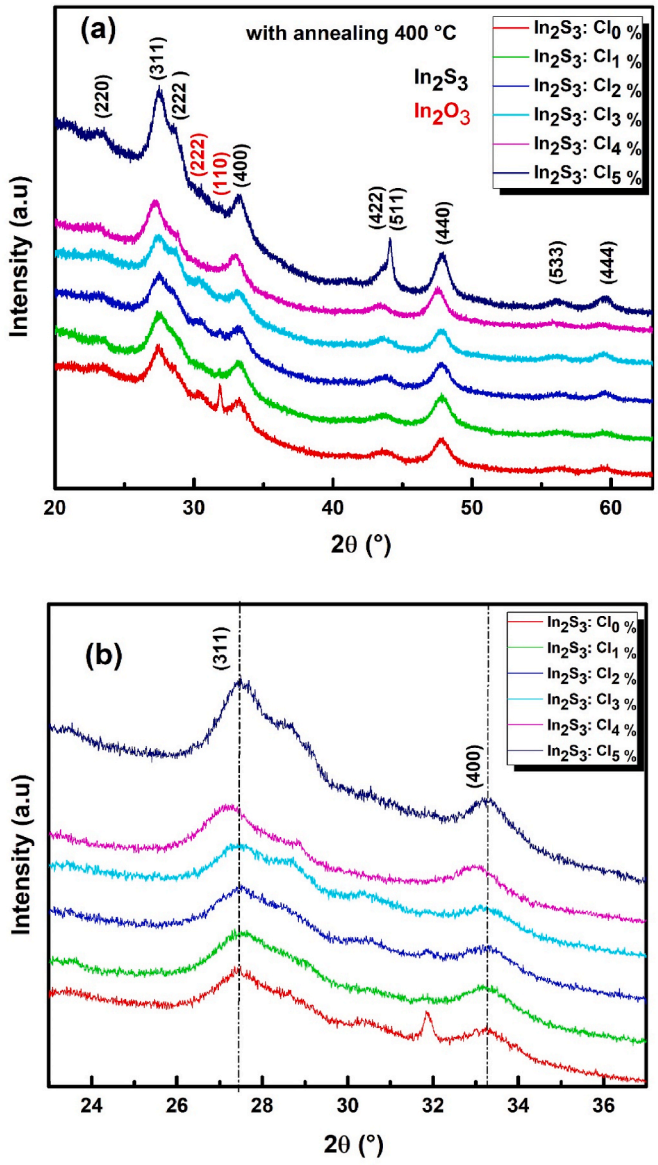

Fig. 1. (a) X-ray diffractograms of In_2S_3:Cl annealed layers, (b) Left shift in the (311) and (400) orientations due to dopant incorporation.

Table 1
Evolution of crystallinity degree, lattice parameter (a), crystallite size (D), bandgap energy (E_g) and Urbach energy (E_U) with the chlorine doping concentration for In_2S_3 films.

In_2S_3:Cl	Crystallinity (%)	a (Å)	D (nm)	E_g (eV)	E_U (eV)
0%	63.03	10.7654	36.37	2.72	416
1%	60.01	10.7624	36.28	2.59	434
2%	55.32	10.7636	36.38	2.79	407
3%	55.15	10.7635	36.43	2.86	407
4%	53.27	10.7609	36.51	2.78	370
5%	54.04	10.7649	36.34	2.92	335

nitrate and 0.1142 g of thiourea in 50 mL of distilled water. For Cl doping, we have added 0, 10, 20, 30, 40 and 50 μL of hydrochloric acid (HCl) to 50 mL of the previously prepared solutions, to obtain 0, 1, 2, 3, 4 and 5% concentrations of Cl, respectively. Then, we cleaned the glass substrates by ultrasound following a specific protocol and keeping their temperature constant at 350 °C during the deposition, which is done by the spray pyrolysis process. Finally, the obtained samples have been annealing in air for 1 h at 400 °C.

2.2. Characterization techniques

Structural, morphological, and optical studies were performed. X-ray diffraction (XRD) was done to infer the structural properties of thin layers ($\lambda_{Cu\text{-}K\alpha} = 1.5406$ Å). On the other hand, we used Raman spectroscopy to study the vibrational modes of the films. Scanning electron microscopy (SEM) was used to study the surface state Quanta 400 FEG ESEM/EDAX Genesis X4M) using an accelerating voltage of 15 kV. SEM images were taken at 50,000- and 100,000-times magnification, while the optical characterization measurements as well as Fourier transformed infrared spectroscopy attenuated total reflectance (FTIR-ATR) with a PerkinElmer Spectrum BX system with a frequency ranging from 4000 to 500 cm^{-1} in transmission mode.

3. Results and discussion

3.1. Structural characterization

Fig. 1a shows the XRD diffractogram of the indium sulfide layers annealed at 400 °C. These patterns show the presence of many peaks which reveal the anisotropic and polycrystalline nature of the samples. All samples crystallize in cubic β-In_2S_3 phase in compliance with the JPDS card No. 00-032-0456. In addition, these patterns reveal In_2O_3 as secondary phase, demonstrating an onset in the conversion of In_2S_3 to In_2O_3. The appearance of In_2O_3 can be explained by the occupation of sulfur vacant sites by oxygen adsorbed during thermal annealing in air. We also note that In_2S_3 tends to rise in the directions (220), (311), (222), (400), (422), (511), (440), (533) and (444), whereas In_2O_3 appears with (222) and (110) orientations. After doping, chlorine addition minimizes sulfur vacant sites which explains the disappearance of In_2O_3. Similar results have been reported in the literature [21,22] for annealed In_2S_3 thin films. The percentage of crystallinity was estimated using the following equation:

$$Crystallinity = \frac{Area\ of\ cristalline\ peaks}{Area\ of\ all\ peaks\ (cristalline + amorphous)} \times 100 \quad (1)$$

The obtained values are shown in Table 1. It is clear that the degree of crystallinity decreases with increasing doping concentration. In general, the intensity of the diffraction peaks decreases sharply with increasing doping concentration, indicating loss of crystallinity due to lattice distortion. When Cl^- ions are incorporated into the periodic crystal lattice of In_2S_3, a strain is induced in the system, resulting in altered lattice periodicity and decreased crystal symmetry [23].

From Fig. 1b we can observe a slight shift of the peaks towards low diffraction angles. Such shift may be due to the presence of a uniform stress (mesh volume dilation) that moves the peaks. This may be an indication of the structural change resulting from the doping and annealing process of the samples. The change in structure may be the cause of the change in the mechanical behaviour (microhardness) of the samples [24].

In order to calculate the crystallite size, Williamson Hall method was used:

$$\beta\ cos\ \theta = \frac{K\lambda}{D} + 4\varepsilon\ sin\ \theta \quad (2)$$

where D is the crystallite size, β full width at half maximum, K = 0.9 and ε the micro strain.

Fig. 2(a,b,c) show the Williamson Hall graphs for In_2S_3:Cl thin films at different chlorine concentrations (0; 1; 2; 3; 4 and 5%). The crystallite size is in the order of 36 nm which indicates that In_2S_3 is a nanomaterial. This value confirms the one found by the Debye-Scherer method determined in a previous work [25].

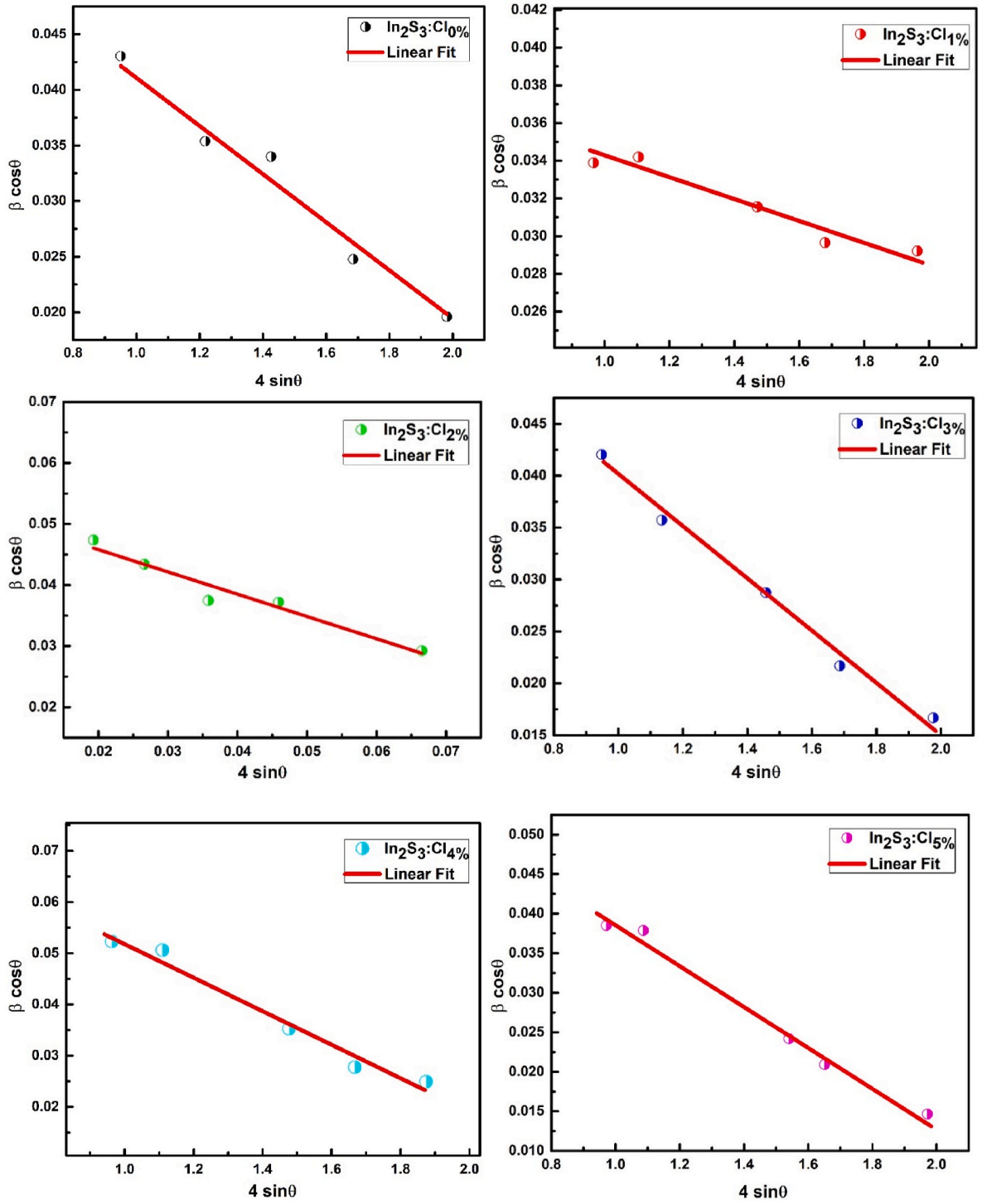

Fig. 2. Williamson-Hall graphs of In_2S_3:Cl films for different chlorine concentrations.

3.2. Raman spectroscopy

Raman spectroscopy was used to characterize the quality of the obtained films. This technique is very strong for the determination of the phase and structure of thin films. Additionally, this system provides information on the mode of vibration within the crystal phase. These modes are strongly dependent on the local atomic arrangement. Fig. 3(a and b) present the Raman spectra of pristine and doped In_2S_3 specimens. The Raman modes are present between 100 and 500 cm^{-1}. It is clear the presence of five broadened peaks and of low intensities situated at 120, 205, 290, 306 and 363 cm^{-1}. These peaks are assigned to the β-In_2S_3 phase [26,27], which agree with the literature [28] confirming the structural characterization as discussed above. The foremost intense peak located at 290 cm^{-1} was identified to the A_1 vibration mode [29].

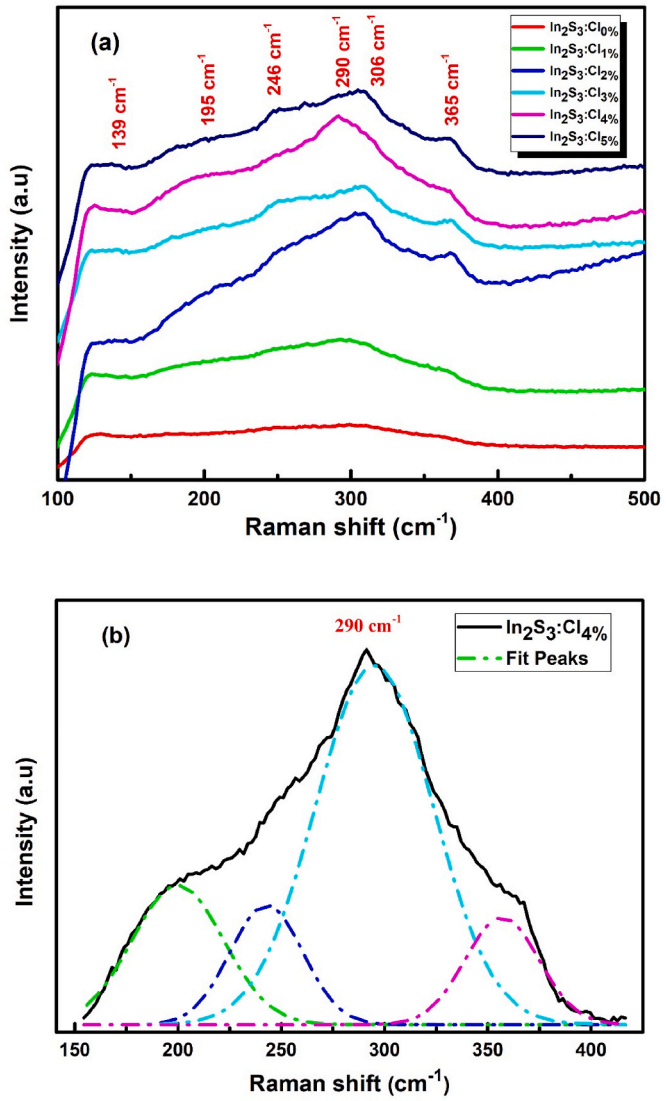

Fig. 3. (a) Raman spectra of In_2S_3:Cl films for different chlorine concentrations, (b) Deconvolution of 290 cm^{-1} peak of In_2S_3:$Cl_{4\%}$ sample.

Raman modes around 120 cm^{-1} and 306 cm^{-1} have been attributed to the A_{1b} vibration [21–25], and the ones near 190 cm^{-1} and 363 cm^{-1} have been identified to be F_{2g} and A_{1g} vibrations, respectively [30,31].

3.3. Morphological study

Fig. 4a depicts the surface morphology of pristine indium sulfide layer. It is clear that the structure of the surface looks grainy with cracks. By using ImageJ software, we calculated the histogram of grain size distribution showed in Fig. 4b. The gaussian fit allows estimating the average of grain size which is around 80 nm. EDS analysis depicted in Fig. 4c was performed to determinate the chemical composition of pristine indium sulfide layer and the results are listed in Table 2. Such results reveal the existence of the pronounced elements: S, In, O and Si. The origin source of Si atoms was the glass substrate, and the origin of O was the glass substrate and some atoms adsorbed on the surface. Besides, the S/In atomic ratio is of the order of 1.35. This indicates that the material is sulfur deficient due to annealing process.

3.4. Fourier transform infrared (FTIR)

In order to investigate the contribution of hydroxyl functions, Fig. 5 shows the FTIR spectra of films of pure and doped In_2S_3, with a chlorine concentration ranging from 0 to 5% after annealing in air at 400 °C. In_2O_3 secondary phase can be found, which is in agreement with the literature [32]. It can be seen also that there are focused absorption bands at around 1300 and 1550 cm^{-1}, as well as an absorption peak at 620 cm^{-1}, which could be attributed to In–S [33]. The located peaks at 3200 cm^{-1} to 3700 cm^{-1} and 1656 cm^{-1} of samples treated at 400 °C have been identified respectively to the O–H stretch vibration of H_2O and the C=O stretch vibration of the absorbed CO_2 [34,35]. In fact, all samples which were exposed to the atmosphere have common absorption of H_2O and CO_2 [32,36]. This suggests that some oxygen-based defects sites and functional groups have been generated [37].

A close observation shows bands at around 3420, 2970, 2200, 1600, 1520, 1390, 872 and 574 cm^{-1}, which did not exist for annealed spectra below 400 °C. These bands might be due to the In–O binding and the formation of In_2O_3, concurring with XRD profiles [38]. Consequently, XRD and FTIR techniques are both collectively consistent with the existence of hydroxyl groups in annealed samples.

3.5. Optical characterizations

3.5.1. Transmission spectra

The transmission spectra of the In_2S_3 and In_2S_3:Cl films, with wavelength ranging from 200 nm to 2500 nm, are shown in Fig. 6. We can deduce that the samples are transparent in the visible and near infrared region. It is clear that all the transmission spectra reveal interference fringes, which indicates a good homogeneity and uniformity of the samples. With the incorporation of chlorine in the matrix of In_2S_3, the transmittance value becomes unchanged up to a doping percentage equal to 3%. Its value is in the order of 70%. Beyond this concentration, the transmittance increases to reach 80%.

3.5.2. Absorption coefficient

We obtained the absorption coefficient α(λ) from the transmittance spectra using:

$$\alpha(\lambda) = \frac{1}{d} ln\left(\frac{1}{T}\right) \quad (3)$$

Fig. 7 shows the absorption coefficient spectra of In_2S_3:Cl. We observe fundamental absorption for $\lambda < 500$ nm, due to transitions from valence band to conduction one. However, when λ exceeds 500 nm this coefficient is reduced to zero.

3.5.3. Band gap

Fig. 8 depicts the evolution of $(\alpha h\upsilon)^2$ versus $(h\nu)$ with different concentrations of chlorine with annealing at 400 °C. It has been observed that the curves give a linear dependence, which means that the optical band gap makes a direct transition. To determinate the gap energy value, we extrapolated the linear part of the evolution of $(\alpha h\upsilon)^2$ compared to $(h\upsilon)$ for a value of zero absorption coefficient. The obtained values were summarized in Table 1. It can be seen that the gap energy value decreases with the increase in the chlorine level up to a minimum value of 2.59 eV for a doping concentration of 1%, then it increases until reaching 2.92 eV for 5% chlorine. The bandgap value decreases for the sample In_2S_3:$Cl_{1\%}$ as a result of dopant states creating a defect tail

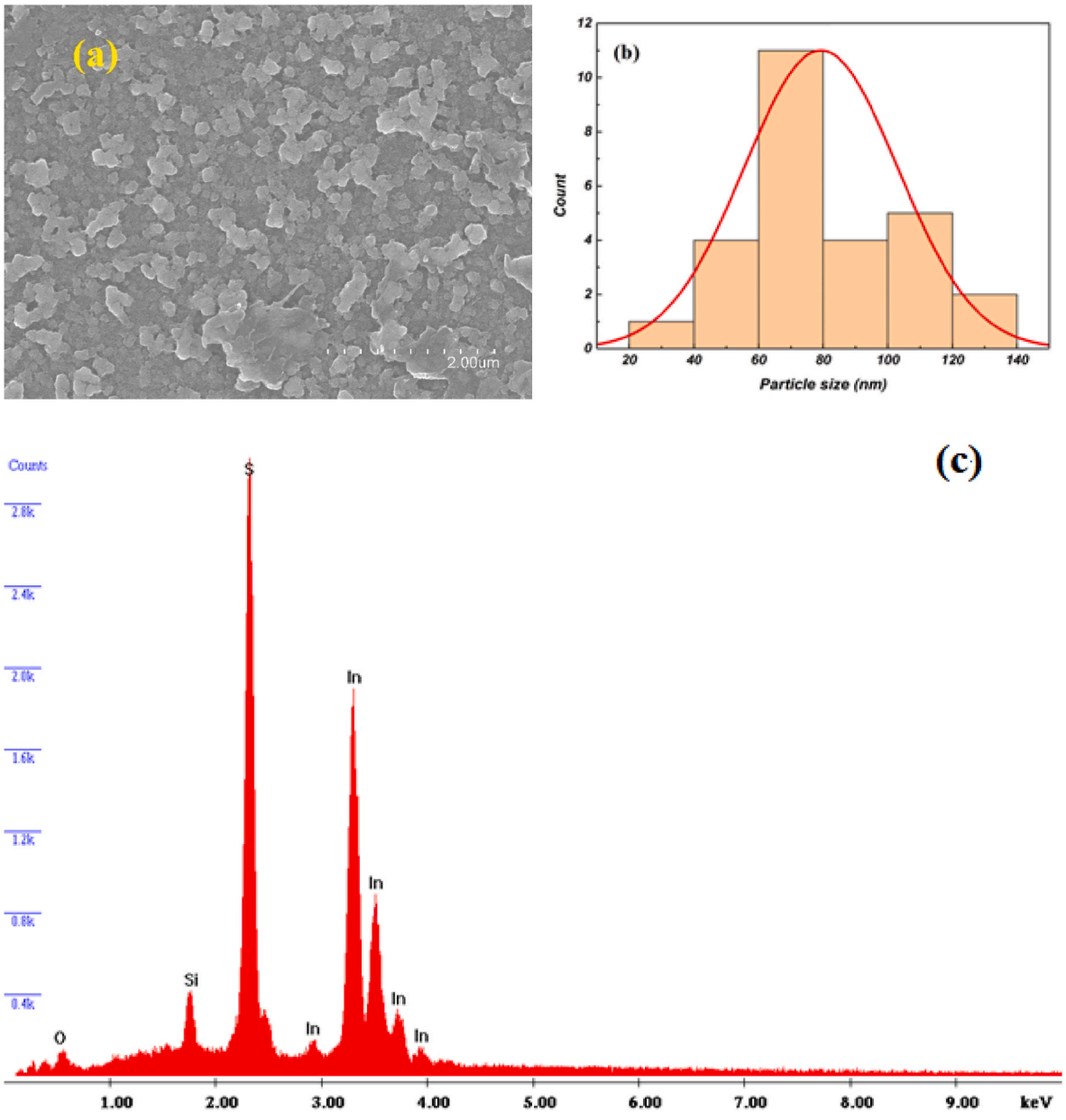

Fig. 4. (a) SEM micrograph, (b) Histogram of grain size distribution, (c) EDS spectrum of undoped In_2S_3 thin layer annealed at 400 °C.

Table 2
Compositional analysis of the pristine In_2S_3film.

Element	Weight %	Atom %	K-Ratio	Z	A	F
S	27.31	57.37	0.2776	1.2176	0.8211	1.0167
In	72.69	42.63	0.6293	0.9089	0.9526	1.0000
Total	100.00	100.00				

named Urbach tail (Cl^- states) [39]. This is characterized by the red shift in absorption spectra illustrated in Fig. 7. The bandgap increase with the rise of doping amount is due to the Burstein Moss effect [40], which is characterized by blue shift in absorption coefficient, causing an increase of charge carrier concentration at high dopant amounts.

3.5.4. *Urbach's energy*

In Fig. 9, we have schematized the evolution of ln(α) versus (hν). Using the linear part, we can collect the energy of Urbach given by the following equation:

$$E_U = \left[\frac{dLn\alpha}{dh\upsilon}\right]^{-1} \quad (4)$$

The deduced values were grouped together in Table 1. It is noted that the Urbach and gap energies are inversely proportional. The Urbach energy evolution proves that the default density decreases with the increase in the concentration of chlorine doping. This subsequently implies the increase in the gap value.

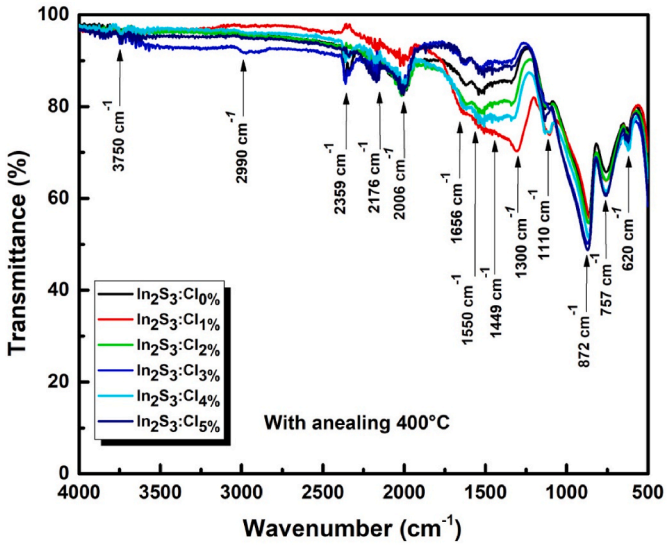

Fig. 5. FTIR spectra of In_2S_3:Cl films for different chlorine concentrations.

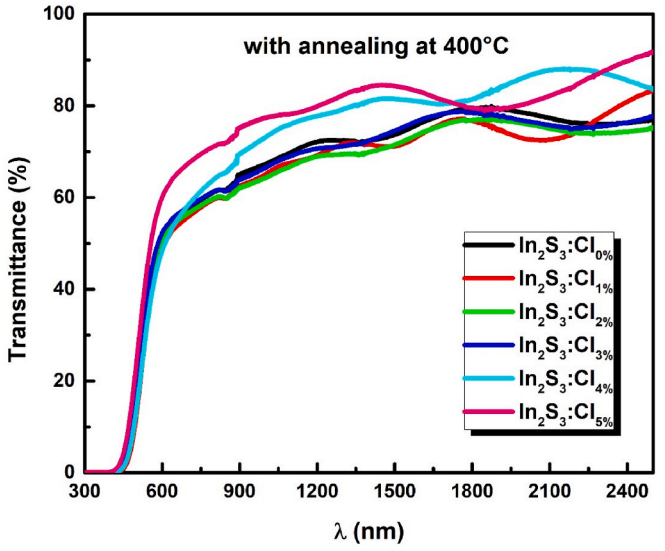

Fig. 6. Transmittance spectra of In_2S_3layers for different Cl concentrations.

4. Conclusion

In_2S_3 layers were deposited on glass substrates using spray pyrolysis process. These layers were treated in air at 400 °C. Structural studies reveal that the prepared layers have a polycrystalline β-In_2S_3 cubic structure, whereas a secondary phase of In_2O_3 was obtained, clearly as a result of the annealing process. In addition, the crystalline size is around 36 nm, while the lattice parameter is around 10.76 Å. From the morphological characterization it was found that the average value of particle size is around 80 nm, which implies that each grain contains approximately two to three crystallites. Optically, 80% in transmittance was obtained for the high doping concentration. The band gap value is affected by the chlorine doping and varies in the range of 2.59–2.92 eV. From the optoelectronic properties studied, it can be concluded that the obtained In_2S_3 films are good candidates for solar cell applications.

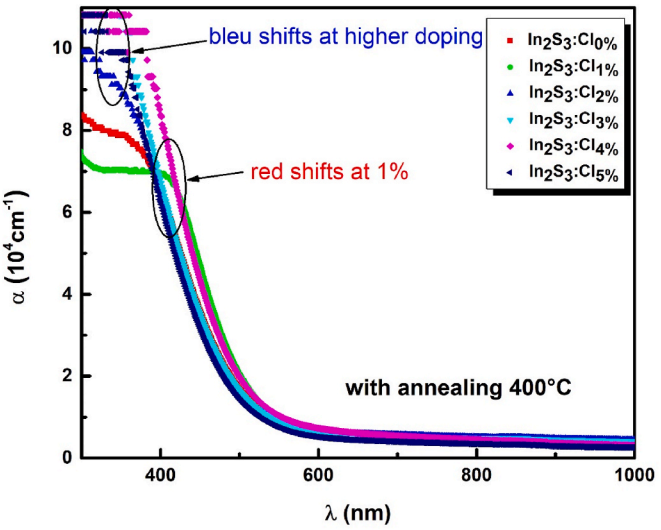

Fig. 7. Evolution of absorption coefficient versus wavelength for In_2S_3layers for different Cl concentrations.

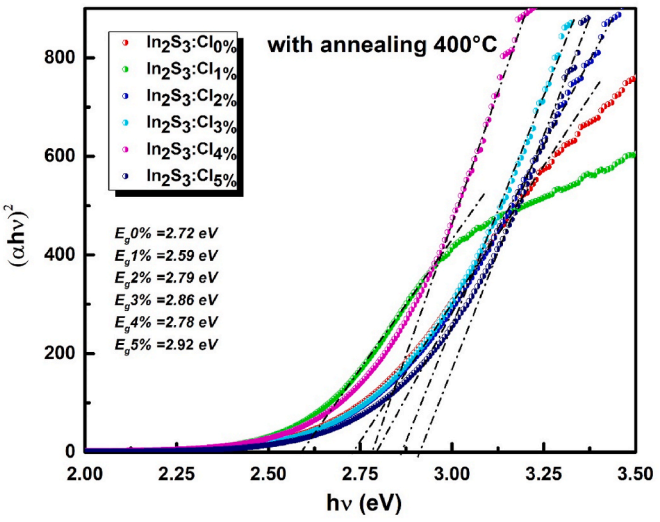

Fig. 8. Variation of $(\alpha h\upsilon)^2$ with $(h\upsilon)$ for In_2S_3:Cl layers.

Credit author statement

M. Toumi: Investigation, Writing- Original Draft, **N. Bouguila**: Supervision, Conceptualization, Writing- Reviewing and Editing, **B. Tiss**: Investigation, **C. Dias**: Supervision, Writing- Reviewing and Editing, **R. C. Veloso**: Investigation, Writing- Reviewing and Editing, **M. Kraini**: Formal analysis, **J. Ventura**: Writing- Reviewing and Editing, **S. Alaya**: Writing- Reviewing and Editing

Declaration of competing interest

The authors declare that they have no known competing financial interests or personal relationships that could have appeared to influence the work reported in this paper.

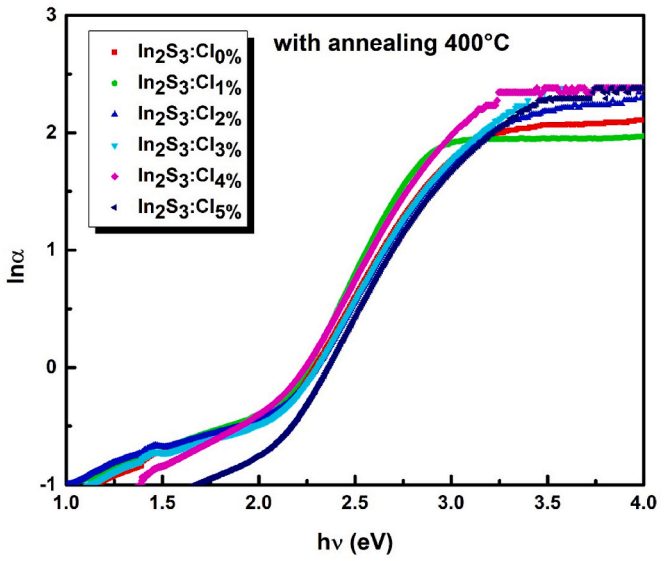

Fig. 9. Variation of lnα with (hυ) for In_2S_3:Cl layers.

Acknowledgments

This work was financially supported by Projects POCI-01-0145-FEDER-031575 and PTDC/ECI-CON/28766/2017—POCI-01–0145-FEDER-028766 funded by FEDER through COMPETE2020—Programa Operacional Competitividade e Internacionalização (POCI), by Project Circular2B - 37_CALL#2 - Circular Construction in Energy-Efficient Modular Buildings financing under the Environment, Climate Change and Low Carbon Economy Programme within the scope of the European Economic Area Financial Mechanism EEA Grants 2014-2021, and by Project PTDC/NAN-MAT/4093/2021 funded by Fundação para a Ciência e a Tecnologia (FCT). R.C. Veloso would like to acknowledge the support of FCT - Fundação para a Ciência e a Tecnologia for the funding of the Doctoral Grant SFRH/BD/148785/2019.

References

[1] X. Meng, Y. Lu, X. Zhang, B. Yang, G. Yi, J. Jia, Appl. Surf. Sci. 258 (2011) 649.
[2] S. Rasool, G. Phaneendra Reddy, K.T. Ramakrishna Reddy, M. Tivanov, V. F. Gremenok, Mater. Today Proc. 4 (2017), 12491.
[3] A.O. Juma, Nucl. Instrum. Methods Phys. Res. Sect. B Beam Interact. Mater. Atoms 385 (2016) 84.
[4] S. Rasool, K. Saritha, K.T.R. Reddy, M.S. Tivanov, A.V. Trofimova, S.E. Tikoto, L. Bychto, A. Patryn, M. Malinski, V.F. Gremenok, Curr. Appl. Phys. 19 (2019) 108.
[5] Y. Ben Salem, M. Kilani, N. Kamoun, Results Phys. 10 (2018) 706.
[6] Y. Ji, Y. Ou, Z. Yu, Y. Yan, D. Wang, C. Yan, L. Liu, Y. Zhang, Y. Zhao, Surf. Coating. Technol. 276 (2015) 587.
[7] R. Souissi, N. Bouguila, A. Labidi, Sensor. Actuator. B Chem. 261 (2018) 522.
[8] Z. Li, X. Tao, Z. Wu, P. Zhang, Z. Zhang, Ultrason. Sonochem. 16 (2009) 221.
[9] Rong Tang, Shuo Chen, Zhuang-Hao Zheng, Zheng-Hua Su, Jing-Ting Luo, Ping Fan, Xiang-Hua Zhang, Tang Jiang, Guang-Xing Liang, Advanced Materials 34 (2022), 202109078.
[10] B. Tiss, M. Erouel, N. Bouguila, M. Kraini, K. Khirouni, J. Alloys Compd. 771 (2019) 60.
[11] SeongYeon Kim, Md Salahuddin Mina, Kiwhan Kim, Jihye Gwak, JunHo Kim, Sustain. Energy Fuels 4 (2020) 362.
[12] N. Kamoun, S. Belgacem, M. Amlouk, R. Bennaceur, J. Bonnet, F. Touhari, M. Nouaoura, L. Lassabatere, J. Appl. Phys. 89 (2001) 2766.
[13] N. Barreau, J.C. Bernede, C. Deudon, L. Brohan, S. Marsillac, J. Cryst. Growth 241 (2002) 51.
[14] R. Jayakrishnan, T. Sebastian, C. Sudha kartha, K.P. Vijayakumar, J. Appl. Phys. 111 (2012), 093714.
[15] T.T. John, S. Bini, Y. Kashiwaba, T. Abe, Y. Yasuhiro, C.S. Kartha, K. P. Vijayakumar, Semicond. Sci. Technol. 18 (2003) 491.
[16] A.S. Cherian, M. Mathew, C. Sudha Kartha, K.P. Vijayakumar, Thin Solid Films 518 (2010) 1779.
[17] Zhenghua Su, Guangxing Liang, Ping Fan, Jingting Luo, Zhuanghao Zheng, Zhigao Xie, Wei Wang, Shuo Chen, Juguang Hu, Yadong Wei, Yan Chang, Jialiang Huang, Xiaojing Hao, Fangyang Liu, Adv. Mater. 32 (2020), 2000121.
[18] Guangxing Liang, Mingdong Chen, Muhammad Ishaq, Xinru Li, Rong Tang, Zhuanghao Zheng, Zhenghua Su, Ping Fan, Xianghua Zhang, Shuo Chen, Adv. Sci. 9 (2022), 2105142.
[19] Shuo Chen, Tianxiang Liu, Mingdong Chen, Muhammad Ishaq, Rong Tang, Zhuanghao Zheng, Zhenghua Su, Xuejin Li, Xvsheng Qiao, Ping Fan, Nano Energy 99 (2022), 107417.
[20] Shuo Chen, Tianxiang Liu, Zhuanghao Zheng, Muhammad Ishaq, Guangxing Liang, Ping Fan, Tao Chen, Tang Jiang, J. Energy Chem. 67 (2022) 508.
[21] V.G. Rajeshmon, N. Poornima, C. Sudha Kartha, K.P. Vijayakumar, J. Alloys Compd. 553 (2013) 23.
[22] J. Raj Mohamed, L. Amalraj, J. Asian Ceram. Soc. 4 (2016) 357.
[23] M. Pal, U. Pal, J.M.G.Y. Jiménez, Pérez-Rodríguez, Nanoscale Res. Lett. 7 (2012) 1.
[24] A.D. Prasetya, M. Rifai, M. Miyamoto, H. Miyamoto, J. Phys. Conf. 1436 (2020), 012113.
[25] M. Toumi, N. Bouguila, R. Souissi, B. Tiss, M. Kraini, S. Alaya, Optik 217 (2020), 164896.
[26] F. Jrad, J. Ben Naceur, R. Ouertani, R. Chtourou, Physica E: Low- dimensional spectrum Systems and Nanostructures 114 (2019), 113585.
[27] H. Tao, S. Tao, G. Dong, Solid State Commun. 137 (2006) 408.
[28] W. Yue, F. Wei, C. He, D. Wu, N. Tanga, Q. Qiao, RSC Adv. 7 (2017), 37578.
[29] E. Aydin, M. Sankir, N.D. Sankir, J. Alloys Compd. 603 (2014) 119.
[30] H. Spasevska, C.C. Kitts, C. Ancora, G. Ruani, Int. J. Photo. 2012 (2012), 637943.
[31] M. Kraini, N. Bouguila, J. Koaib, C. Vázquez-Vázquez, M.A. López-Quintela, S. Alaya, J. Electron. Mater. 45 (2016) 5936.
[32] M. Kraini, N. Bouguila, J. El Ghoul, I. Halidou, S.A. Gomez-Lopera, C. Vázquez-Vázquez, M.A. López-Quintela, S. Alaya, Mater Electron 6 (2015) 3136.
[33] C. Huang, Y. Hong, X. Yan, L. Xiao, K. Huang, W. Gu, K. Liu, W. Shi, RSC Adv. 46 (2016), 40137.
[34] M. Kraini, N. Bouguila, I. Halidou, A. Timoumi, S. Alaya, Mater. Sci. Semicond. Process. 16 (2013) 1388.
[35] V. Pyragas, V. Lisauskas, K. Sliuziene, B. Vengalis, Lith. J. Phys. 51 (2011) 47.
[36] D. Dastan, S.L. Panahi, N.B. Chaure, J. Mater. Sci. Mater. Electron. 27 (2016), 12291.
[37] S.L. Panahi, D. Dastan, N.B. Chaure, Adv. Sci. Lett. 22 (2016) 941.
[38] Z. Gao, B. Xu, M. Ma, A. Feng, Y. Zhang, X. Liu, Z. Jia, G. Wu, Compos. B Eng. 179 (2019), 107417.
[39] S. Duman, Gurbulak, Dogan, S. Ozcelik, J Phys Conf Ser 707 (2016), 012027.
[40] N. Khoshsirat, N.A.M. Yunus, J. Electron. Mater. 45 (2016) 5721.